Available online at www.sciencedirect.com

ScienceDirect

Geochimica et Cosmochimica Acta 284 (2020) 156–172

Geochimica et Cosmochimica Acta

www.elsevier.com/locate/gca

Experimental investigation of lithium isotope fractionation during kaolinite adsorption: Implications for chemical weathering

Wenshuai Li, Xiao-Ming Liu

Department of Geological Sciences, University of North Carolina, Chapel Hill, NC 27599, USA

Received 23 January 2020; accepted in revised form 23 June 2020; available online 2 July 2020

Abstract

The feedback between CO_2 sources and sinks through chemical weathering is one of the important reasons why Earth has maintained a habitable climate for over four billion years. The lithium (Li) isotopic system is a promising tracer of silicate weathering, but the mechanisms causing its isotope fractionation during weathering remain ambiguous. Here, we performed batch experiments of Li adsorption to one of the common clay minerals -kaolinite in three sets, including the time-series, pH-dependent, and concentration-control sets. Our results demonstrate that the liquid-solid Li isotope fractionation reaches up to 36‰, with up to 99% initial Li being adsorbed on kaolinite. The magnitudes of Li adsorption and isotope fractionation increase with reaction time, and reach the steady-state after ~1000 min. The magnitude of Li isotope fractionation increases with the adsorption ratio of Li, in positive relationships with solute pH and ionic strength. At constant solute pH = 8.5 and ionic strength of 0.001 M, the adsorption ratio and isotope fractionation of Li on kaolinite reach the maximum with the lowest initial Li concentration of 2 μM. In experiments, Li is removed by kaolinite as the inner-sphere and/or outer-sphere complexes, likely followed by structural occupation as supported by incomplete desorption. We model the Li isotope fractionation in all three sets, which can be best described by Rayleigh distillation models. In summary, significant Li isotope fractionation occurs following a kinetic law in closed-systems during adsorption on kaolinite. Adsorption-driven isotope fractionation conforms to a kinetic solid-liquid isotope fractionation factor $\alpha \sim 0.992$, consistent with theoretical ion-desolvation between complexed and dissolved ions ($\alpha = 0.9925$, Hofmann et al., 2012). This study reveals a vital kinetic role of clay uptake in Li isotope fractionation during chemical weathering, suggesting rapid forward adsorption reaction versus relatively slow backward reaction. The dominance of the kinetic mechanism over the equilibrium mechanism further explains field observations from rivers worldwide. Given above, the outcome of this study calls for additional attention on low-temperature kinetic Li isotope fractionation at Earth's surface and further refinement of quantitative models using geological Li records to trace weathering and reconstruct climate.

Keywords: Li isotope; Kaolinite; Clay; Adsorption; Incorporation; Weathering; Kinetic fractionation

1. INTRODUCTION

Chemical weathering, defined as the chemical dissolution of rocks and minerals on Earth's surface, transfers essential nutrients from the source region into the oceans, eventually modulating global climate over geological time scales (e.g., Kump et al., 2000; Tabor et al., 2002; John et al., 2003; Willenbring and Von Blanckenburg, 2010; Heimsath et al., 2012). Lithium (Li) isotope fractionations have been used to examine long-term chemical weathering, which contributes to the transfer of terrestrial nutrients to oceans, and is known to modulate the global carbon cycle and climate change by carbonate mineral formation (e.g.,

E-mail addresses: wenshuai@live.unc.edu (W. Li), xiaomliu@unc.edu (X.-M. Liu)

https://doi.org/10.1016/j.gca.2020.06.025
0016-7037/

Dosseto et al., 2015; Tomascak et al., 2016; Penniston-Dorland et al., 2017). As chemical weathering is typically incongruent, soil formation serves as a critical Li sink and is accompanied by significant Li isotope fractionations. Because the Li isotopic system is less sensitive to carbonate weathering and biological activities, it is a unique weathering tracer whose behavior is dominantly regulated by the changes in silicate weathering intensity (e.g., Huh et al., 1998, 2001; Pistiner and Henderson, 2003; Hathorne and James, 2006). Stable Li isotopic compositions (reported as per-mil variations from the stable isotopic composition of an international Li standard by the notation of δ^7Li [‰] = $\{[(^7Li/^6Li)_{sample}/(^7Li/^6Li)_{standard}] - 1\} \times 1000‰$) preserved in sedimentary records such as carbonate sediments thus provide insights into long-term feedbacks between climate and weathering (Penniston-Dorland et al., 2017; Pogge von Strandmannet al., 2017a). Marine δ^7Li records have been examined to interpret changes in weathering, such as (i) Li budget balances between riverine and submarine reverse weathering fluxes during the Cenozoic (e.g., Misra and Froelich, 2012; Vigier and Goddéris, 2015), (ii) considerable changes in denudation regimes as influenced by temperature (climate)-controlled oceanic sinks during the Cenozoic (Li and West, 2014), (iii) variations in river and hydrothermal fluxes during the Jurassic Oceanic Anoxic Events (e.g., Pogge von Strandmann et al., 2013; Lechler et al., 2015), and (iv) dramatic changes in Li inputs from continental weathering during the period of the Hirnantian glaciation (Pogge von Strandmannet al., 2017b).

Numerous studies have focused on Li isotope geochemistry within riverine systems to understand weathering processes, and possible links between Li isotope fractionation and chemical weathering has been vigorously debated. Pioneering research (Huh et al., 1998) suggested the substantial correlation between river Li isotope fractionation and weathering intensity. Following this notion, Li fluxes have been positively correlated to weathering rates, whereas riverine δ^7Li values have been shown to reflect "weathering intensity" (Kisakürek et al., 2004), "weathering congruency" (Pogge von Strandmann et al., 2008), and "weathering efficiency" (Pogge von Strandmann and Henderson, 2015). A study on Icelandic rivers suggested that silicate weathering mass fluxes and rates are difficult to infer based on the δ^7Li values of riverine sediments derived from multiple sources (Vigier et al., 2009). In comparison, studies of the Orinoco River (Huh et al., 2001), Mackenzie River (Millot et al., 2010), and the Amazon River (Dellinger et al., 2015, 2017) have shown close relationships between river Li isotopic composition and physicochemical indexes defined as "weathering regimes", which depend on interrelated factors including weathering rates, temperature, and climate (Pogge von Strandmann et al., 2010; Wang et al., 2015; Weynell et al., 2017; Gou et al., 2019; Bohlin and Bickle, 2019). Riverine Li isotopic ratios could be controlled by the water–rock interaction time in both subsurface and river (e.g., Wanner et al., 2014; Liu et al., 2015). Specifically, studies on the Lena River imply that riverine δ^7Li depends on the balance between rock dissolution and soil formation, rather than climatic and weathering regimes (Murphy et al., 2019). No apparent correlation was found between riverine δ^7Li values and traditional weathering proxies such as Si content in streams draining monolithology (Liu et al., 2015). It is expected since dissolved Si is not conservative in the riverine system, while Li is largely conservative (Wilke and Dayal, 1982; Bencala et al., 1990). Investigations on the Ganges-Brahmaputra River and the high relief areas of the Yangtze River indicated that Li isotopes reflect weathering congruency and intensity (Pogge von Strandmannet al., 2017b; Ma et al., 2020). However, there is no universal correlation between riverine dissolved δ^7Li and weathering rates, and a second weathering step resulting in high dissolved δ^7Li has been found within floodplain sediments compared with mountainous regions (e.g., Bagard et al., 2015; Pogge von Strandmannet al., 2017b; Bohlin and Bickle, 2019; Ma et al., 2020).

Using Li isotopes to trace chemical weathering and climate relies on our ability to link isotope fractionations to soil formation. The processes may affect riverine Li isotopic ratios and can be addressed by well-constrained laboratory experiments: (i) how Li isotope fractionation between clays and its surrounding solutions responds to climate, and corresponding tectonic controls, and (ii) which mechanism (kinetic vs. equilibrium) regulates Li isotope behavior during clay uptake during chemical weathering. Commonly, the equilibrium fractionation mechanism verified for metal isotopes (e.g., Zn, Guinoiseau et al., 2016; Ca, Brazier et al., 2019) has been applied for Li isotopes in low-temperature fluid-clay interactions. The Li isotope fractionation, along with clay formation, is critical as ^{6}Li is preferentially hosted into octahedral sites in clay structures. All else being equal, the Li incorporation into high coordination number environments such as lattice octahedrons prefers the lighter isotope, suggested by the equilibrium stable isotope fractionation theory (Schauble, 2004). Supportively, it agrees with the result from the theoretical prediction, revealing that ^{7}Li is preferentially left in the aquo-complex (Yamaji et al., 2001; Bogatko et al., 2013).

Previous sorption experiments have indicated that Li isotope fractionations vary due to differences in clay mineralogy, i.e., >10‰ for gibbsite, 1–3‰ for ferrihydrite and chlorite, ~7‰ for kaolinite, and close to 0‰ for smectite and illite (Pistiner and Henderson, 2003; Millot and Girard, 2007). At starting Li concentrations ([Li] of 1 to 12 M) far in excess of natural concentrations, the intercalation of Li into gibbsite results in isotope fractionation between dissolved (aqueous, 'aq') and adsorbed ('ad') phases ($\Delta^7Li_{aq\text{-}ad} = \delta^7Li_{aq} - \delta^7Li_{ad}$) (Wimpenny et al., 2015). The magnitude of isotope fractionation depends on the availability of octahedral sites in gibbsite structure and aqueous anion speciation. Synthesis of smectite at temperatures ranging from 90 °C to 250 °C produces substantial variations in Li isotope fractionations (Vigier et al., 2008), which has been interpreted as the equilibrium isotope fractionation dependent on bond stiffness, temperature, and aqueous chemistry (e.g., pH and anionic composition). Based on ^{7}Li NMR, Hindshaw et al. (2019) synthesized Mg-rich layer silicates and calculated site-specific δ^7Li of $-21.5 \pm 1.1‰$, $-0.2 \pm 1.9‰$ and $15.0 \pm 12.3‰$ for clay

octahedral, outer-sphere and pseudo-hexagonal sites, respectively. To date, field studies and corresponding quantitative models assumed different equilibrium fractionation factors in a wide range of 13 ‰ to 30‰ between clays and water (e.g., Hathorne and James, 2006; Misra and Froelich, 2012; Bouchez et al., 2013; Wanner et al., 2014; Bohlin and Bickle, 2019; Gou et al., 2019). Notably, recent batch basalt alternation experiments in ambient conditions by Pogge von Strandmann et al. (2019) produced Li isotope data that can be fitted by Rayleigh models, hinting a possible kinetic control. In addition, theoretical calculations have recognized the kinetic controls on Li isotope fractionations during cation mineral exchange (Hofmann et al., 2012). Clay synthesis experiments indicated a potential rate-dependent kinetic isotope effect superimposed on the equilibrium Li isotope fractionation at high pH and ambient temperatures (Hindshaw et al., 2019). Here, we performed closed-system batch experiments at room temperature to assess the mechanisms and quantify the magnitudes of Li isotope fractionations during adsorption onto a common clay mineral kaolinite under constrained laboratory conditions.

2. MATERIALS AND EXPERIMENT SETUP

2.1. Material preparation

We produced deionized water (18.2 MΩ) from a Milli-Q (MQ) element system (Direct-Q 3UV) for experimental preparations and used analytical-grade (>99.9% purity) LiCl, $FeCl_3$, NaCl, NaOH, and sodium hexametaphosphate (NaHMP) from Acros Organic™. Commercially available hydrochloric acid (HCl) was purified in-house by double distillation in a Teflon® sub-boiling still (Savillex™, NC, USA) and diluted to the required molarities. Our study focuses on Li adsorption onto one common secondary clay kaolinite to reach the first-order analogy to weathering environments. Here, we used the well-characterized high-defect kaolinite (KGa-2) reference material obtained from the Clay Mineral Society (www.clays.org, VA, USA). After immediate water cooling at 30 ^{0}C, the solid product was recovered and separated by centrifugation (30 min, 12,000 rpm), and dried in an oven at 60 ^{0}C for over two days. The N_2-BET specific surface area of kaolinite (KGa-2) (0.1–1 μm size) has been reported in a previous study (Brazier et al., 2019), where the BET-N_2 value of kaolinite is 21.1 m^2/g. It is comparable to the certified value (the Clay Mineral Society, http://www.clays.org/), where the BET-N_2 value of KGa-2 is 23.5 m^2/g.

Critically, samples were processed to extract clay-sized fractions (0.1–1 μm), and removed surface impurity or labile components to avoid possible errors in chemical analysis. Here, we employed the washing protocol modified from Guinoiseau et al. (2016) and Brazier et al. (2019). Clay samples were immersed overnight in a mixture of NaHMP (dispersant, 10 mM) and MQ water, and the clay fractions (0.1–1 μm size) were recovered based on Stokes' law. In brief, the NaHMP-extracted clay slurry was introduced into acid-cleaned centrifuge tubes using a pipette, then centrifuged at 10,000 rpm for 0.5 h, and the supernatant was discarded. A 0.5 M NaCl solution was then added to the slurry, centrifuged at 10,000 rpm for 0.5 h, and the supernatant discarded. After that, MQ water was added, centrifuged at 10,000 rpm for 0.5 h, and the supernatant discarded. The water rinse process was repeated to remove excess salts and NaHMP until the concentrations of Na and P in eluent were below the detection limits of the ICP-MS instrument at sub-ppb levels to ensure that the clay was thoroughly clean to perform adsorption experiments. Finally, recovered clays were dried in a vacuum oven at 60 °C, powdered in an agate mortar, and stored at 4 °C for experiments. Before the experiments, we examined the possible influence of Li released from the clay structure using control groups to which no Li was added (Fig. S1). We found the total Li release from the clay under the studied conditions to be negligible (less than 0.1 ng/mL), comparing to total Li loads of 14–7000 ng/mL used in these experiments.

2.2. Experimental setup

To evaluate the influence of common environmental factors on the isotope fractionation between aqueous and adsorbed Li, we designed three individual sets of kaolinite adsorption experiments under ambient temperature conditions: (i) the time-series experiments, in which we tracked aqueous chemistry as a function of reaction time for up to 15 days at pH of 7 with the constant starting Li concentration of 10 and 75 μM; (ii) the pH-dependent experiments, in which we varied the solute pH from 3 to 10 with the constant starting Li concentration of 75 μM; and (iii) the concentration-control experiments, in which we varied the starting Li concentration from 2 to 1000 μM at a pH range of 3 to 10. We note that KGa-2 kaolinite displays negative surface charges over the studied pH range of 3–10 (Fig. S2a), leading to the electrostatic attraction to dissolved cations. Batch experiments were performed in 50 mL centrifuge tubes filled with the clay slurry (10 g/L) and continuously stirred at 150 rpm in a temperature-controlled water bath shaker (Thermo Scientific™). LiCl solutions were prepared with pre-set background electrolyte (NaCl) to evaluate the effect of ionic strength (IS) on surface complexation (i.e., chemisorption or inner-sphere complexation versus physisorption or outer-sphere complexation), and 10 g/L kaolinite suspensions were added. Experiments were performed for the pH-dependent and concentration-control sets with equilibration for 24 h, which is long enough to achieve the steady-state as supported by the time-series sets. The applications of solute IS = 0.001 M and 0.1 M are intended to represent natural freshwater and brines, respectively. In the following text, we defined pH ≥ 7 as "high pH" and pH < 7 as "low pH", and IS = 0.001 M as "low IS" and IS = 0.1 M as "high IS".

Desorption experiments were carried out in the same clay-solution batch-systems to investigate Li complexation modes on kaolinite. We performed two kaolinite adsorption experiments as the control sets, which were equilibrated for 15 days at IS = 0.001 M, pH = 8.5 (Kaolin (1)), and 4.3 (Kaolin (2)), and initial Li concentration of

75 μM. Then, clay slurry after supernatant removal was treated with three individual desorption steps for 15 days. In Step (1), solute IS was increased from 0.001 M to 0.1 M NaCl. In Step (2), 0.0001 M Hexamminecobalt (III) chloride ($[Co(NH_3)_6]Cl_3$) was added into the clay-solution system (Brazier et al., 2019). In Step (3), solute pH was decreased from 8.5 to 4.3 through dropwise acidification using 0.001 M HCl, and compared with the control group. The same sampling procedure as that used for the adsorption experiments was applied. Both control and desorption sets were performed in triplicates to ensure the reproducibility and accuracy.

Over the course of experiments, we did not employ any pH buffers in order to minimize undesired complexation and particle aggregation. We maintained the solute pH at $\pm$ 0.2 by regular monitoring using a Thermo Scientific^{TM} Orion Star A221 portable pH meter; the pH was adjusted by doping with trace amounts of HCl and NaOH as necessary. All reagents were prepared from distilled acids and MQ water to avoid contamination. Supernatants were filtered through 0.22 μm cellulose acetate syringe filters (Thermo Scientific^{TM}) and transferred into acid-cleaned centrifuge tubes. The suspensions were centrifuged at the end of the experiments, and processed kaolinite was rinsed with water, air-dried, crushed, and transferred into borosilicate vials. Samples were stored at 4 °C for chemical analysis. Solute Li concentrations are reported as [Li] in the text. The Li isotopic compositions of the dissolved and solid phases (adsorbed Li) were analyzed and are reported relative to the international standard (see Analytical Methods) in a δ notation (δ^7Li_{aq}, dissolved Li; δ^7Li_{ad}, adsorbed Li). And, $\Delta Li_{aq\text{-}ad}$ represents the isotope fractionation between dissolved Li and adsorbed Li.

3. ANALYTICAL METHODS AND MODELS

3.1. Zeta potential analysis

To analyze the interfacial electrical fields of kaolinite, aliquots of clay dispersions from each experimental set were transferred into centrifuge tubes and re-suspended with a 10-min ultrasonic treatment. The electrophoretic mobility of the clays was measured based on their direction and velocity along with applied electric fields in a Malver^{TM} Zetasizer Nano ZS90 equipped with a red (633 nm) laser and converted to zeta potentials based on the Smoluchowski equations. At least three replicate analyses were performed for each sample in ambient conditions to estimate the reproducibility and uncertainties (Fig. S2a).

3.2. Infrared spectroscopy

To determine the changes of Li complexation on kaolinite surfaces at different pH, we measured the attenuated total reflectance Fourier transform infrared (ATR-FTIR) spectra of reacted solids (Fig. S2b). All ATR-FTIR spectra were collected in the 400–4000 cm^{-1} range under ambient temperature, using a BRUKER^{TM} Alpha spectrometer equipped with an ATR attachment. Air-dried samples were directly coated on a diamond crystal surface and pressed tightly by a pressure head. Twenty-four scans were collected at a resolution of 2 cm^{-1}, and background spectra were acquired in clay-free areas of the diamond sample mount. The ATR-FTIR spectra data were collected and processed using the OPUS software.

3.3. Element analysis

Elemental analyses were performed on an Agilent^{TM} 7900 quadrupole inductively coupled plasma mass spectrometer (Q-ICP-MS) at the Plasma Mass Spectrometry Lab of the University of North Carolina, Chapel Hill. Concentration calibration curves were acquired by using external standards with a series of multi-element reference solutions of known concentrations (prepared by the ICP standard solutions, Inorganic Ventures^{TM}). Internal standards, including Be, Ge, Ph, In, Ir, and Bi, were added for instrumental drift correction. Data quality was controlled based on repeated analyses of international reference materials BHVO-2 (Hawaiian basalt) and SLRS-5 (Ottawa Britannia water) (element compositions certified by the United States Geological Survey and the National Research Council of Canada, respectively) (Table S1). Relative standard derivation (RSD) $<$ 3% can be achieved, and digestion yields were 100 $\pm$ 5%. The percentage of Li adsorption onto clays was calculated based on staring and final solute Li concentrations and was reported in wt. % (weight percent).

3.4. Column purification

Prior to Li isotopic analyses, solid and liquid samples were processed in different ways. For liquid samples, filtrates were evaporated and re-dissolved in 0.2 M HCl solutions. The solid residues were completely digested by successive acid baths in Teflon beakers (Savillex^{TM}) using concentrated HF-HNO_3-HCl mixture. The Li fraction was purified by two-step cation-exchange chromatography (Bio-Rad^{TM} AG50W X-8 resin) using HCl as the eluent. In brief, samples were evaporated to dryness and converted to HCl form in 0.2 M HCl. Samples were first passed through a cycle of the first column, which is filled with 2.4 mL AG50-X8 200–400 mesh cation-exchange resin (Bio-Rad^{TM}). After sample loading, 60 mL of 0.2 M HCl was added slowly to the column at an average elution rate of ca. 2 min mL^{-1}. The Li fraction between 19 and 44 mL was collected. Collected 1st Li fraction was dried down, and re-dissolved in 1 mL 0.5 M HCl, and passed through another cycle of the second column, filled with 2 mL AG50-X8 200–400 mesh resin (Bio-Rad^{TM}). The Li fraction between 4 and 16 mL was collected, with Li/Na $>$ 1. We achieved satisfactory Li yields (~100%), and the total procedural blanks (0.004 ng Li) far less than the experimental Li loads had negligible impacts on the isotopic analyses. Because the matrix elements-to-Li ratios were less than 1, matrix interferences during isotope measurements can be avoided.

3.5. Lithium isotope analysis

Liquid samples were analyzed on the Thermo Scientific^{TM} Neptune Plus multi-collector inductively coupled plasma mass spectrometer (MC-ICP-MS) at the Rutgers University. A concentration matched unprocessed NIST L-SVEC standard was measured before and after each sample to monitor instrument drift. The standard-sample normalization approach was adopted to correct for instrumental mass discrimination. Before isotopic analyses, the Li collected after chromatographic separation was evaporated to dryness, converted into nitric form, and diluted to 20 ppb Li in 2% HNO_3. Prepared Li solutions of 20 ppb were analyzed that, utilizing a Teledyne Cetac Aridus II and X-type Ni skimmer cone, yielded a signal exceeding 18 V on δ^7Li signals with an acid blank of <150 mV. The high sensitivity of the instrument allows small samples to be processed through ion chromatography, which enables column calibrations to be stable. A standard–sample–standard bracketing method was used, and signals matched to within 5%. Measured isotopic ratios are reported in δ notation, as the deviation in parts per thousand of the measured $^7Li/^6Li$ from the to the NIST RM 8545 (L-SVEC) standard (Tomascak et al., 1999). The long-term external uncertainties (two standard deviations, 2SD) of Li isotopic analyses by our MC-ICP-MS instrument are 0.6‰ (W.-Li et al., 2019). The granite (GSP-2, -0.64 ± 0.6‰) and basalt (BHVO-2, 4.7 ± 0.6‰) USGS standards were measured, and the values fall within the uncertainties of previously reported data (Lin et al., 2016; Liu and Li, 2019) (Table S2) The δ^7Li_{ad} values of adsorbed Li were corrected by the deduction from the original structural Li composition in kaolinite lattice (0.2 ± 0.6‰) following Eq. (1):

$$\delta^7Li_{ad} = \frac{[Li]_{total} \times \delta^7Li_{total} - [Li]_{kao} \times \delta^7Li_{kao}}{[Li]_{ad}} \quad (1)$$

where $[Li]_{total}$ and δ^7Li_{total} are the Li concentration and isotopic composition of reacted kaolinite, and $[Li]_{kao}$ and δ^7Li_{kao} are those of cleaned kaolinite. The isotope fractionation between adsorbed Li and aqueous Li, Δ^7Li was defined as (Eq. (2)):

$$\Delta^7Li = \delta^7Li_{ad} - \delta^7Li_{aq} \quad (2)$$

For calculations, analytical errors were propagated using the following equation (Eq. (3)):

$$E = \sqrt{(c_1\Delta W_1)^2 + (c_2\Delta W_2)^2 + \cdots + (c_n\Delta W_n)^2} \quad (3)$$

where ΔE notates the absolute error of additive functions, c is the multiplicative factor, and W represents the additive function input. In the text, we employed the long-term analytical uncertainties for reported data, and the error of 0.6‰ keeps constant.

3.6. Kinetic models

Kinetic modeling of the time-series adsorption data is shown in Fig. S3. The overall sorption rates and migration processes of the adsorbate at solid-water interfaces are controlled by surface characteristics and the resistance of the solid particles to diffusion. Therefore, the utilization of proper kinetic models can provide instructive information on the mechanism of adsorption processes such as mass transfer and chemical reaction during the entire adsorption process. Here, we use the pseudo-second-order model, the pseudo-first-order model, the intra-particle diffusion model, and the Elovich model to explore Li adsorption kinetics. Linear correlation coefficients (R^2) near or equal to 1, indicating consistency between predicted values and the experimental data, suggest that a particular model effectively describes the observed Li adsorption kinetics. One to three adsorption could be generally distinguished: the first represents the initial rapid to instantaneous adsorption of external adsorbate, the second is the rate-limited adsorption stage, and the third is the equilibrium stage, in which adsorption slows significantly due to the low adsorbate concentrations remaining in the dissolved phase.

The pseudo-first-order model (Lagergren, 1898) is based on solid capacity, which primarily involves ion-exchange physisorption in a homogeneous liquid-solid system, and is generally expressed in a linearized form as follows (Eq. (4)).

$$1/q_t = k/tq_t + 1/q_e \quad (4)$$

where q_e is the equilibrium concentration of Li adsorbed on clays or adsorption capacity, q_t is the dissolved Li concentration at time t, and k_1 is the first-order model constant. Pseudo-first-order reactions are those that should occur at some higher order (>1), but occur as a first-order since the concentration of one reactant is high relative to the other(s).

The pseudo-second-order model (Ho and McKay, 1999) is based on a limited adsorbate concentration, which mainly involves chemisorption in a liquid-solid system, and is generally expressed in a linearized form as follows (Eq. (5)).

$$t/q_t = 1/k_2(q_e)^2 + t/q_e \quad (5)$$

where q_e is the adsorbed amount of Li at equilibrium, q_t is the adsorbed amount of Li at time t, and k_2 notates the second-order model constant. Pseudo-second-order reactions assume solid-phase adsorption, and that the rate-limiting step is chemisorption involving valence forces through the sharing or exchange of electrons between sorbent and sorbate.

The Elovich model (Low, 1960) is another rate-based equation derived from adsorption capacity, which mainly involves chemisorption in heterogeneous systems, and is generally expressed in a linearized form as follows (Eq. (6)).

$$q_t = \beta Ln(\alpha\beta) + \beta Int \quad (6)$$

where q_t is the amount of Li adsorbed on clays at the time t, α denotes the initial Li adsorption rate, and β represents the desorption constant related to the surface coverage and the activation energy for chemisorption. The integration of the rate equation with the same boundary conditions as the pseudo-first- and second-order equations (as mentioned above) becomes the Elovich equation.

Alternatively, the intra-particle diffusion model (Srihari and Das, 2008) describes adsorption from a mechanistic

point of view, which mainly involves diffusion mechanisms, and is expressed in a linearized form as follows (Eq. (7)).

$$q_t = k_3 t^{0.5} \quad (7)$$

where q_t is the amount of Li adsorbed on clays at the time t, and k_3 is the intra-particle rate constant. The overall adsorption process may indeed be controlled by one or more steps, e.g., film or external diffusion, pore diffusion, surface diffusion and adsorption on the pore surface, or a multi-linear combination of steps. Our results show that the pseudo-second-order model achieves R^2 values closest to 1 and thus best describes the adsorption kinetics, assuming that the main rate-limiting step is chemisorption involving covalent forces through the sharing or exchange of electrons between Li^+ and clay surface hydroxyl groups.

3.7. Isotherm adsorption models

Adsorption isotherms describe chemical equilibrium and the interaction between adsorbate and adsorbent. The equilibrium state is reached when the adsorbate concentration in the dissolved phase is in the dynamic balance with adsorbent concentration. Here, we employed the widely used Langmuir (Eq. (7)) and Freundlich (Eq. (8)) isotherm adsorption models to fit the experimental data in concentration-control sets (Fig. S4). Importantly, we note that the Langmuir and Freundlich models describe macroscopic data only, and do not definitively prove sorption mechanisms. Therefore, the mentioned modeling approaches may imply a single adsorption process or an interplay of multiple adsorption processes.

The Langmuir model (Langmuir, 1918) implies that adsorption takes place with a mono-molecular layer arrangement on adsorbent surfaces, and there is no interaction between the adsorbed molecules. A linearized form of the Langmuir isotherm model can be expressed as follows (Eq. (8))

$$1/Q_e = 1/Q_0 + 1/Q_0 K_L C_e \quad (8)$$

Where q_e is the amount of solute adsorbed per unit weight of adsorbent, Q_0 is the theoretical maximum adsorption capacity, C_e notates the equilibrium Li concentration (mg/L), and K_L represents the Langmuir constant.

The Freundlich isotherm model (Freundlich, 1928) suggests that molecules are adsorbed as a mono-molecular layer or multilayer on heterogeneous adsorbent surfaces, and there is an interaction between adsorbed molecules. A Linearized form of the Freundlich isotherm model can be expressed as follows (Eq. (9))

$$LogQ_e = LogK_f + 1/nLogC_e \quad (9)$$

where Q_e is the amount of solute adsorbed per unit weight of adsorbent, C_e is the equilibrium concentration of solute in the bulk solution; n and K_f are Freundlich constants (information about bond energies between the adsorbent and the metal ions.). Generally, the energy distribution of the real solid surface is not uniform. In this case, the Freundlich adsorption model presumes that adsorption occurs on the non-uniform surface, which may be closer to the real surface of clays in nature.

4. RESULTS

4.1. Characterization of Li adsorption and desorption

A total of 127 batch experiments were performed in three individual experimental series. Clay adsorption results are summarized in Tables 1–3, and shown in Fig. 1. Clay desorption results are provided in Table S3, and shown in Fig. S5a. In the time-series experiments, the percentage of Li adsorbed onto kaolinite ranges from 37.3% to 91.4% (10/75 μM Li) at solute IS of 0.001 M, and from 43.3% to 82.8% (10/75 μM Li) at solute IS of 0.1 M. A rapid increase in the magnitude of Li adsorption was observed at the early stage of reaction (stage I, within 1000 min), and reached the equilibrium status until the end of experiments (15 days) (stage II, Fig. 1). Kaolinite surface coverages range from 0.04 to 0.24 μM Li/m^2. In the pH-dependent experiments, the percentage of Li adsorbed onto kaolinite increases with pH from 3 to 10, ranging from 11.2% to 91.3% at solute IS of 0.001 M, and from 11.2% to 96.2% at solute IS of 0.1 M. Kaolinite surface coverages range from 0.04 to 0.36 μM Li/m^2. In the concentration-control experiments, the percentage of adsorption on kaolinite decreases with incremental [Li] of 2 to 1000 μM, and ranges from 11.2% to 99.2%. The K adsorption decreases with increases in solute IS from 0.001 M to 0.1 M at pH < 7, and remains near-consistent at high/low IS at pH > 7. Kaolinite surface coverages range from 0.01 to 1.14 μM Li/m^2. In the desorption experiments, the percentage of Li adsorption at pH = 8.5 and IS = 0.001 M is 90.2% to 92.5% (Kaolin (1)), and the percentage of Li adsorption at pH = 4.3 and IS = 0.001 M is 65.1% to 68.9% (Kaolin (2)). With IS increasing to 0.1 M (Step (1)) or addition of 0.0001 M $[Co(NH_3)_6]Cl_3$ (Step (2)) at pH = 8.5, there is no apparent change (<1%) in Li adsorption ratios. With pH decreasing from 8.5 to 4.3 in the same batch (Step (3)), Li adsorption ratio changes from ~90% to 62.4% to 70.2%, higher than these of Kaolin (2).

4.2. Characterization of Li isotope fractionation

The isotopic compositions of aqueous and adsorbed Li are provided in Tables 1-3, and displayed in Figs. 2 and 3. The Li isotope data of clay desorption are provided in Table S3, and displayed in Fig. S5b. Long-term analytical uncertainty of 0.6‰ (2SD) is used for all reported data (W.-Li et al., 2019). The isotopic compositions of initial LiCl and pristine kaolinite are 5.8 ± 0.6‰ and 0.2 ± 0.6‰, respectively. In all sets, lighter isotopes were preferentially adsorbed. In the time-series experiments, aqueous isotopic compositions of Li (10/75 μM Li) ranges from 10.1‰ to 26.0‰ at solute IS of 0.001 M, and from −9.3‰ to 22.2‰ (10/75 μM Li) at solute IS of 0.1 M. A transit positive isotope shift in aqueous Li from the LiCl signal was observed at the early stage of reaction (stage I, within 1000 min), and approached the steady status until the end of experiments (15 days) (stage II, Fig. 2) at IS of 0.001 M. Such a feature did not occur at IS of 0.1 M. In the pH-dependent experiments, Li isotope compositions of liquids remained in the fluids (δ^7Li_{aq}) range from 6.0 ‰ to 28.7 ‰ at IS of 0.001 M, and from 5.9‰ to 29.0‰

Table 1
Kaolinite Li adsorption and isotope fractionation in time-series sets.

pH	Initial [Li] (uM)	Final [Li] (uM)	2SD	Sorption ratio (%)	Solution δ^7Li (‰)	IS (M)	Time (h)
7.0	10	1.9	0.2	81.4	20.1	0.001	5 min
		1.7	0.5	82.9	n.d.	0.001	10 min
		1.7	0.4	82.9	20.6	0.001	20 min
		1.4	0.3	85.7	n.d.	0.001	30 min
		1.3	0.3	87.1	24.5	0.001	1 h
		1.1	0.3	88.6	24.1	0.001	3 h
		1.1	0.3	88.6	n.d.	0.001	5 h
		1.0	0.1	90.0	n.d.	0.001	10 h
		0.9	0.0	91.4	25.2	0.001	1 d
		0.9	0.2	91.4	n.d.	0.001	3 d
		0.9	0.2	91.4	25.1	0.001	7 d
		0.9	0.3	91.4	26.0	0.001	15 d
7.0	10	2.7	0.6	72.7	11.2	0.1	5 min
		2.4	0.3	75.7	n.d.	0.1	10 min
		2.3	1.2	76.8	19.6	0.1	20 min
		2.1	0.9	78.6	n.d.	0.1	30 min
		2.0	0.5	80.0	20.2	0.1	1 h
		1.9	0.7	81.2	20.5	0.1	3 h
		1.9	0.3	81.1	19.9	0.1	5 h
		1.9	0.1	81.4	n.d.	0.1	10 h
		1.9	0.5	81.5	20.0	0.1	1 d
		1.7	0.3	82.7	20.7	0.1	3 d
		1.7	0.4	82.8	22.2	0.1	7 d
		1.9	0.3	81.5	20.0	0.1	15 d
7.0	75	47.0	5.6	37.3	n.d.	0.001	5 min
		42.5	7.2	43.3	10.1	0.001	10 min
		38.3	2.3	48.9	n.d.	0.001	20 min
		35.7	1.1	52.4	n.d.	0.001	30 min
		31.4	2.2	58.1	14.5	0.001	1 h
		32.3	1.7	57.0	n.d.	0.001	3 h
		32.2	3.0	57.1	n.d.	0.001	5 h
		30.9	1.6	58.7	n.d.	0.001	10 h
		30.9	4.3	58.9	12.4	0.001	1 d
		31.6	5.4	57.9	n.d.	0.001	3 d
		31.2	4.9	58.5	12.3	0.001	7 d
		30.9	3.4	58.9	12.3	0.001	15 d
7.0	75	42.5	5.1	43.3	n.d.	0.1	5 min
		38.0	6.5	49.3	9.3	0.1	10 min
		34.6	1.1	53.9	n.d.	0.1	20 min
		33.5	5.4	55.4	n.d.	0.1	30 min
		29.9	4.8	60.1	12.0	0.1	1 h
		28.5	3.4	62.0	n.d.	0.1	3 h
		28.4	4.1	62.1	n.d.	0.1	5 h
		28.3	1.4	62.2	n.d.	0.1	10 h
		28.1	3.9	62.6	11.8	0.1	1 d
		27.9	4.7	62.9	n.d.	0.1	3 d
		27.9	2.9	62.9	11.6	0.1	7 d
		27.9	2.7	62.9	11.6	0.1	15 d

Note 1: The percentage of adsorbed Li (%) is calculated from (initial [Li]-final [Li])/initial [Li] (in uM) in average. Two standard deviation (2SD) is calculated from the data of the experiment in triplicates. The analytical uncertainty of Li isotope analysis is 0.6‰ (2SD) (W.-Li et al., 2019). The Li isotope composition of LiCl is 5.8 ± 0.6‰.
Note 2: n.d. means not determined.

at IS of 0.1 M. It can be seen that δ^7Li_{aq} exhibit positive correlations with the adsorption ratio of Li, in line with increases in solute pH in the studied pH range of 3 to 10. In the concentration-control experiments, δ^7Li_{aq} ranges from 6.1‰ to 39.7‰, and adsorbed Li isotopic composition δ^7Li_{aq} ranges from −4.3‰ to 3.7‰. The Li isotope fractionation between adsorbed and aqueous Li exhibits a wide variety of −35.8‰ to −1.6‰, in negative relationships with the percentage of Li adsorption. In the desorption experiments of kaolinite, δ^7Li_{ad} at pH = 8.5 and IS = 0.001 M is 2.2‰ to 2.5‰ (Kaolin (1)), and $^7Li_{ad}$ at pH = 4.3 and IS = 0.001 M is −3.7‰ to 3.1‰ (Kaolin (2)). With IS increasing to 0.1 M (Step (1)) or addition of 0.0001 M $[Co(NH_3)_6]Cl_3$ (Step (2)) at solute pH = 8.5, there is no

Table 2
Kaolinite Li adsorption and isotope fractionation in pH-dependent sets.

pH	Initial [Li] (uM)	Final [Li] (uM)	2SD	Sorption ratio (%)	Solution δ^7Li (‰)	IS (M)	Time (h)
3.7	75	66.6	7.3	11.2	6.0	0.001	24
4.4		65.9	1.3	12.2	6.1	0.001	
5.6		55.3	0.6	26.3	9.0	0.001	
6.6		39.0	2.7	48.0	10.8	0.001	
7.0		27.9	1.4	62.9	12.4	0.001	
7.5		14.1	1.9	81.2	18.2	0.001	
8.5		3.5	0.6	95.4	28.7	0.001	
9.1		6.5	1.4	91.3	25.0	0.001	
3.7	75	66.6	16.7	11.2	5.9	0.1	24
4.4		66.5	20.6	11.3	5.9	0.1	
5.6		59.7	7.2	20.4	8.3	0.1	
6.6		41.7	6.3	44.4	11.0	0.1	
7.0		30.7	0.3	59.1	11.8	0.1	
7.4		13.4	0.7	82.1	20.6	0.1	
8.5		2.9	0.2	96.2	29.0	0.1	
9.1		5.8	0.6	92.2	25.2	0.1	

Note 1: The percentage of adsorbed Li (%) is calculated from (initial [Li]-final [Li])/initial [Li] (in uM) in average. Two standard deviation (2SD) is calculated from the data of the experiment in triplicates. The analytical uncertainty of Li isotope analysis is 0.6‰ (2SD) (W.-Li et al., 2019). The Li isotope composition of LiCl is 5.8 ± 0.6‰.

apparent change (within the analytical uncertainty of 0.6‰, W.-Li et al., 2019) in Li adsorption ratios. With solute pH decreasing from 8.5 to 4.3 in the same batch (Step (3)), δ^7-Li_{ad} changes to a range of 0.9‰ to 0.2‰, while is greater than these of Kaolin (2) by ~3‰ at the same pH.

5. DISCUSSION

The isotopic compositions of aqueous Li and adsorbed Li in the adsorption experiments exhibit wide variations from −4.3 to 39.7‰ under various conditions. Absolute Li isotope fractionations between aqueous and adsorbed Li in the same condition are heterogeneous (-35.8‰ to −1.6‰), positively correlated with the percentage of Li adsorption. We provide a conceptual model describing possible complexation mechanisms for Li adsorption onto kaolinite (Fig. 4). Generally, there are two adsorption sites available of different proportions on clay surfaces: (i) edge surfaces (the surface charge from hydroxyls) and (ii) basal surfaces (permanent structural charge). The pH-dependence of the edge surfaces can be verified by our zeta potential analysis, which shows increasing surface negative charge density with increasing pH (Fig. S2a). Commonly, Li^+ could be adsorbed as inner-sphere complexes (chemisorption) on clay edge surfaces, and as outer-sphere complexes (physisorption) on clay basal surfaces. Our infrared spectra further confirm the site-specific Li adsorption onto clay edge surfaces, which is supported by attenuated hydroxylic Al-O (aluminols), Si-O (silanols), and Al-O-Si vibrations from alkaline to acidic conditions (Fig. S2b). Using ^{7}Li NMR, Wimpenny et al. (2015) suggested that adsorbed Li may be incorporated into gibbsite structure. Since the kaolinite sample used here is poorly-ordered and a large number of defects exist on its edge surfaces, we infer that adsorbed Li might be incorporated into the defects on edge surfaces of kaolinite samples. Two possible mechanisms (path 1, kinetic, and path 2, equilibrium) might influence the isotopic compositions of dissolved Li (Fig. 4). In the following sections, we propose and evaluate the mechanisms of Li adsorption on clays and its isotope fractionation during clay adsorption, then address potential interfacial paths controlling Li isotopic behavior. Further implications for tracing chemical weathering using Li isotopes are provided at the end.

5.1. Li adsorption mechanism

Dissolved Li concentrations decrease parabolically as the reaction proceeds and depend on solute pH, initial [Li], and IS (Fig. 2). Time-series experiments show linear correlations between t/[Li] and t (t being time; $R^2 > 0.999$) and are best fitted by pseudo-second-order kinetics; rate constants can thus be calculated from the slopes of the t/[Li] versus t relationships (Fig. S3). Such kinetic patterns suggest a rate-limiting step and single characteristic adsorption that is probably dominated by chemisorption rather than physisorption (Fig. S3). The Langmuir model simulates the sorption isotherms better at high pH/IS, and the Freundlich model fits the data better at low pH and IS. This indicates that the binding energy is homogenous on the kaolinite surface at high pH and IS, but heterogeneous at low pH and IS. These results are consistent with the gradual deprotonation and activation of surface hydroxyl groups from acidic to alkaline conditions (Tombácz and Szekeres, 2006), as confirmed by zeta-potential analyses (Fig. S2a). This interpretation is also supported by Li-Na exchanges on the kaolinite surface at high IS (as supported by the deduction from adsorption; Tables 1–3). Moreover, as prepared, the kaolinite samples have finite specific surfaces and cation sorption capacities. Thus, adsorption at high pH is better described by the Langmuir rather than the Freundlich model because the Freundlich model assumes exponentially increasing adsorption amount. Combining the results from the kinetic and isotherm models, we

Table 3
Kaolinite Li adsorption and isotope fractionation in concentration-control sets.

pH	Initial [Li] (uM)	Final [Li] (uM)	2SD	Sorption ratio (%)	Solution δ^7Li (‰)	Adsorbed δ^7Li (‰)	IS (M)	Time (h)
4.3	2	0.6	2.2	72.0	11.6	0.8	0.001	24
4.3	5	2.7	0.9	45.8	9.5	−0.3		
4.3	10	6.7	1.1	32.7	8.6	−0.6		
4.3	25	17.9	4.3	28.4	6.4	−1.5		
4.3	50	42.8	6.8	14.4	6.4	−2.5		
4.3	75	65.9	5.3	12.2	6.1	−3.1		
5.5	5	0.8	0.1	84.3	16.9	1.1	0.001	24
5.5	10	2.2	0.4	78.0	14.4	0.5		
5.5	25	11.7	1.5	53.3	11.2	0.2		
5.5	50	33.0	5.9	34.1	8.1	−0.4		
5.5	75	55.3	9.4	26.3	n.d.	n.d.		
5.5	100	81.1	15.4	18.9	6.2	−1.1		
5.5	125	104.8	12.6	16.1	n.d.	n.d.		
5.5	5	1.0	0.3	79.9	19.1	0.4	0.1	24
5.5	10	3.1	0.7	69.3	14.9	0.6		
5.5	25	10.5	2.7	58.0	n.d.	n.d.		
5.5	50	30.5	7.0	39.1	9.4	−1.2		
5.5	75	59.7	10.2	20.4	n.d.	n.d.		
5.5	100	85.2	6.8	14.8	8.5	−2.7		
5.5	125	110.9	23.3	11.2	n.d.	n.d.		
6.5	10	0.8	0.2	92.1	16.1	1.4	0.001	24
6.5	25	7.0	1.3	72.1	11.9	−0.2		
6.5	50	22.5	4.7	55.0	n.d.	n.d.		
6.5	75	41.3	4.1	45.0	9.4	−0.8		
6.5	100	61.5	8.0	38.5	n.d.	n.d.		
6.5	125	79.0	12.6	36.8	8.5	−1.9		
6.5	5	0.5	0.1	90.1	23.2	2.1	0.1	24
6.5	10	1.8	0.6	82.4	18.4	1.0		
6.5	25	9.4	3.7	62.2	14.8	0.7		
6.5	50	23.7	3.8	52.5	13.9	0.1		
6.5	75	41.7	4.6	44.4	11.0	−0.5		
6.5	100	61.1	7.9	38.9	9.5	−1.4		
6.5	125	85.2	13.6	31.8	9.4	−1.4		
7.5	25	2.1	0.2	91.6	26.1	3.7	0.001	24
7.5	50	6.3	1.4	87.5	20.4	1.0		
7.5	75	14.1	2.4	81.2	18.2	0.7		
7.5	100	24.1	1.7	75.9	15.9	0.1		
7.5	125	48.6	11.2	61.1	14.3	−0.2		
7.5	250	178.4	5.4	28.6	n.d.	n.d.		
7.5	500	419.6	67.1	16.1	n.d.	n.d.		
7.5	1000	875.0	105.0	12.5	n.d.	n.d.		
8.5	25	0.2	0.0	99.2	39.7	3.9	0.001	24
8.5	50	1.6	0.3	96.7	28.4	3.2		
8.5	75	6.5	0.1	91.3	25.0	2.3		
8.5	100	20.6	4.1	79.4	22.6	0.5		
8.5	125	34.2	2.4	72.6	n.d.	n.d.		
8.5	250	95.4	24.8	61.8	10.8	−2.3		
8.5	500	291.3	110.7	41.7	n.d.	n.d.		
8.5	1000	771.0	131.1	22.9	7.7	−4.3		

Note 1: The percentage of adsorbed Li (%) is calculated from (initial [Li]-final [Li])/initial [Li]. Two standard deviation (2SD) is estimated from the experiment in triplicates.
Note 2: Analytical uncertainty of Li isotope analysis is 0.6‰ (2SD) (W.-Li et al., 2019). The Li isotope composition of LiCl salt is 5.8 ± 0.6‰. n.d. means not determined.

suggest that the inner-sphere rather than outer-sphere complexation dominates the adsorbed Li pool with increasing pH and IS. Hence, monolayer adsorption and chemisorption dominate in such aqueous conditions.

Increased Li adsorption with increasing pH at both low and high IS suggests that inner-sphere complexation becomes important at pH > 5. Furthermore, identical Li adsorption ratio at high (high Na^+) and low IS (low Na^+) at pH > 7 supports that the replacement of physically adsorbed Li^+ (outer-sphere complex) by Na^+ becomes negligible at pH > 7 (Fig. 2). Such a feature implies that inner-sphere complexation dominates in circumneutral to alkaline

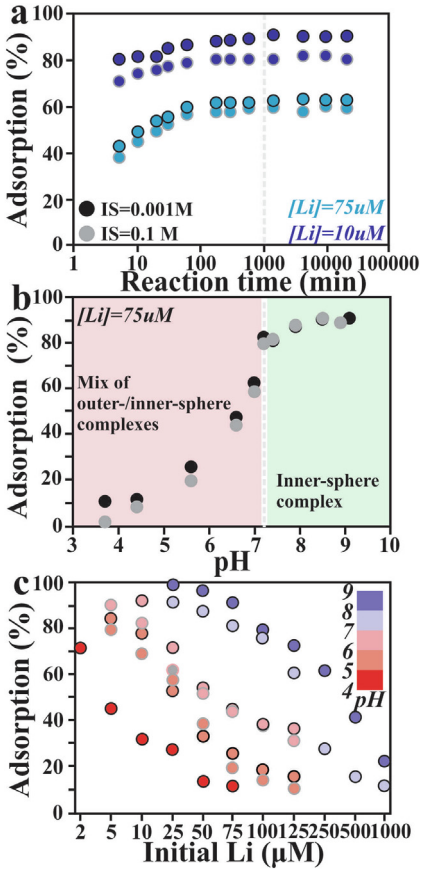

Fig. 1. Kaolinite Li adsorption in the time-, pH-, and concentration-series experiments. (a) Kaolinite Li adsorption with the initial [Li] = 10 and 75 μM in the time-series sets for kaolinite. (b) Kaolinite Li adsorption with initial [Li] = 75 μM in the pH-dependent sets (pH ~ 4–10). (c) Kaolinite Li adsorption at a pH range of ~4–10 in the concentration-control sets ([Li] = 2–1000 μM). The colors of light blue and dark blue denote time-series sets with [Li] of 75 μM and 10 μM, respectively. The colors of black and grey represent solute IS of 0.001 M and 0.1 M, respectively. The colors from red to purple show increasing solute pH from 3 to 10 in concentration-control sets. The analytical uncertainties on Li adsorption ratios using Q-ICP-MS ([Li], RSD < 2‰) are smaller than the symbol sizes.

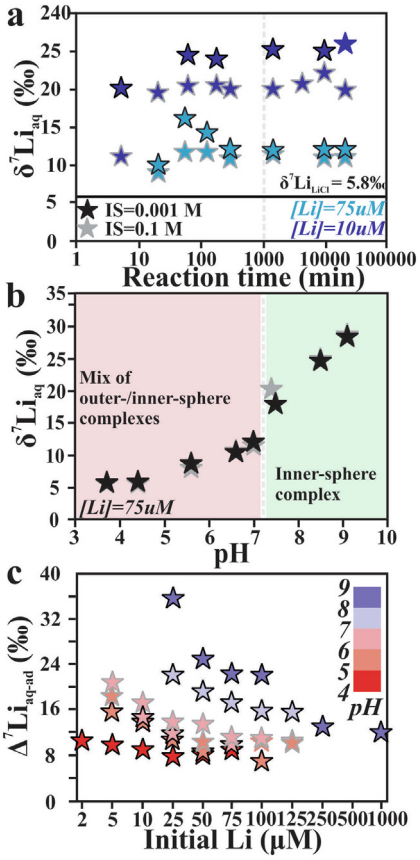

Fig. 2. Solute Li isotopic compositions in the time-, pH-, and concentration-series experiments during kaolinite adsorption. (a) Li isotopic signals of aqueous phases at initial [Li] = 10 μM and 75 μM in the time-series experiments at pH 7 for kaolinite. The aqueous Li isotopic composition at IS of 0.001 M and [Li] = 75 μM reached the maximum value before decreasing to the equilibrium state. (b) Li isotopic signals of aqueous phases at [Li] = 75 μM in the pH-dependent experiments (~4–10) for kaolinite. (c) Net Li isotope fractionation between aqueous phases and adsorbed phases at a pH range of ~4–10 in the concentration-control sets ([Li] = 2–1000 μM) for kaolinite. The initial isotopic composition of added LiCl (δ^7Li_{LiCl}) was 5.8‰. The colors of light blue and dark blue denote time-series sets with [Li] of 75 μM and 10 μM, respectively. The colors of black and grey represent solute IS of 0.001 M and 0.1 M, respectively. The colors from red to purple show increasing solute pH from 3 to 10 in concentration-control sets. Long-term analytical uncertainty on δ^7Li (2SD = 0.6‰) is smaller than the symbol size.

conditions, which cannot be easily replaced by excess Na^+ of high ionic potential (Strawn and Sparks, 1999). This conclusion is further supported by the negative charge accumulation on clay surface in response to increasing solute pH (Fig. S2a), which provides deprotonated hydroxyls located on clay edge surfaces for direct bonding (Guinoiseau et al., 2016). According to the changes in adsorption ratios at high and low IS, the concentration-controlled experiments show that both physisorption and chemisorption occur at low pH < 7, and chemisorption dominates at high pH. This interpretation is supported by the isothermal models (Fig. S4) and consistent with increased occurrence of inner-sphere complexation with increasing solute pH from 3 to 10.

Our infrared data reveal that Li adsorption occurs exclusively on basal and edge surfaces (Fig. S2b), particularly the edge surfaces in high-pH/IS conditions, as supported by the pH dependence of edge site availability. After adsorption as outer- or inner-sphere complexes, Li is closely surrounded by oxygen atoms of water molecules (outer-sphere complex) or oxygen atoms of hydroxyls on clay surfaces that are bound to the central metal atom, displacing water molecules (inner-sphere complex). The extended X-ray absorption fine structure (EXAFS) of the local atomic coordination of Cd, Zn, and Cu complexed on clay surfaces indicates monodentate-mononuclear, monodentate-binuclear, or bidentate-mononuclear binding at high pH (e.g., Peacock and Sherman, 2004; Lee et al., 2004;

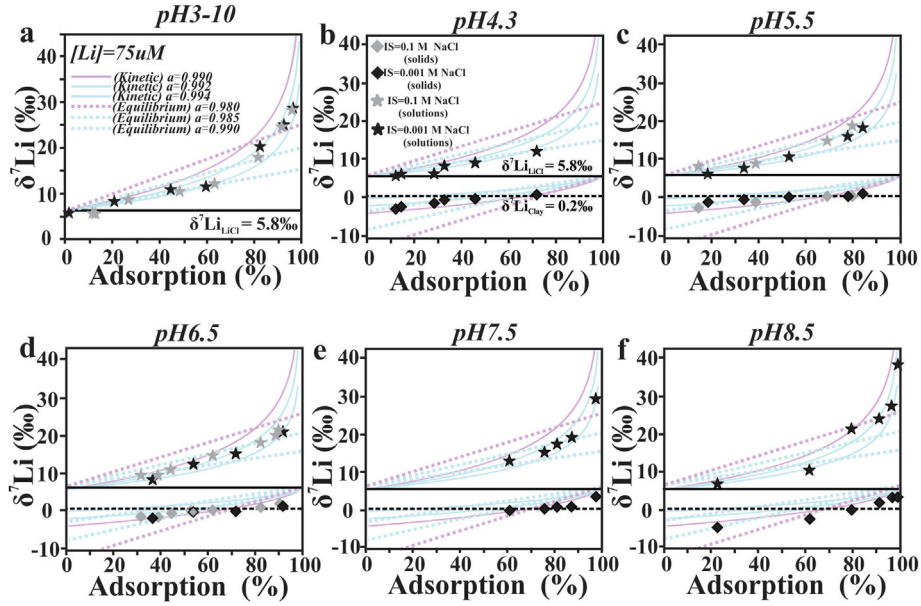

Fig. 3. Modeling of the observed Li isotope fractionations during kaolinite adsorption. Rayleigh distillation (kinetic, solid curves, $\alpha = 0.990$ to 0.994) and equilibrium models (dashed curves $\alpha = 0.980$ to 0.990) of closed-system isotope fractionation in (a) the pH-dependent experiments and (b–f) the concentration-control experiments over a range of pH values. The initial δ^7Li values of LiCl (solid black line) and pristine kaolinite (dashed black line) are 5.8 ± 0.6‰ and 0.2 ± 0.6‰, respectively. The isotopic compositions of dissolved and adsorbed Li phases are marked by stars and diamonds, respectively. The colors of black and grey represent solute IS of 0.001 M and 0.1 M NaCl, respectively. Long-term analytical uncertainty on δ^7Li (2SD = 0.6‰) is smaller than the symbol size. Modeled fractionation patterns are shown in the plot by lines in light blue (the lowest one), cyan (the optimal one), and purple (the highest one).

Vasconcelos et al., 2008). However, the adsorption feature of Li^+ may be different from the above divalent metal ions due to its strong hydration (Rudolph et al., 1995). The interlayer spaces in kaolinite seem to be inaccessible to aqueous Li^+ due to strong interlayer hydrogen bonds. However, solid-state ^{7}Li NMR and scanning electron microscopy analyses suggest Li incorporation into gibbsite octahedral vacancies (i.e., intercalation in interlayers) and Li adsorption with excess Li (Wimpenny et al., 2015). Therefore, our isotopic data aid in the understanding of dominant controls on Li isotope fractionation during soil formation, and the magnitude of isotope fractionation for structural substitution and surface adsorption needs further differentiation.

5.2. Li isotope fractionation mechanism

The Li isotopic trends observed in the time-series experiments with [Li] = 75 μM (i.e., rise-fall-plateau at low IS, and rise-plateau at high IS; Fig. 2) correspond to different Li isotopic behaviors, reflecting the influences of chemisorption and physisorption. The former trend was not observed in experiments with [Li] = 10 μM at low or high IS (Fig. 2), which may suggest the preferential occupation of strong hydroxyl sites via inner-sphere complexation. We infer that the isotopic composition of weakly fixed Li (i.e., outer-sphere complexes) is easily erased by cationic competition with Na, and that only inner-sphere complexes are preserved at high IS, as reported for the successive involvement of different binding sites for Cu and Zn adsorption on kaolinite (Heidmann et al., 2005; Guinoiseau et al., 2016). Indeed, surface complexation models estimate the isotope fractionation factors of Zn in outer-sphere complexes on kaolinite basal surfaces to be about 0.18‰, regardless of aqueous chemistry (Guinoiseau et al., 2016). In comparison, the degree of equilibrium isotope fractionation of Ca^{2+} as outer-sphere complexes on soil phyllosilicates (kaolinite, montmorillonite, and muscovite) is related to the permanent negative charge of Ca on clay basal surfaces and/or in interlayers (Brazier et al., 2019). It is difficult to estimate the isotope fractionation factor of outer-sphere Li complexes using surface models due to a lack of thermodynamic parameters. Here, we infer that reversible Li adsorption (i.e., physisorption without direct bonding) follows an equilibrium isotopic mechanism, as proposed to describe a similar Zn isotope pattern during adsorption onto Mn oxyhydroxides (Bryan et al., 2015).

To decipher between equilibrium and kinetic isotope fractionation mechanisms, we predict the Li isotopic compositions of absorbed (δ^7Li_{ad}) and dissolved Li (δ^7Li_{aq}) using the Rayleigh distillation (kinetic) and batch steady-state (equilibrium) models in closed systems, which can be expressed as (Eqs. (10) and (11)):

$$\delta^7Li_{ad} = \left(\frac{\alpha \times \delta^7Li_{LiCl} + 1000 f_{Li} \times (\alpha - 1)}{\alpha(1 - f_{Li}) + f_{Li}}\right);$$
$$\delta^7Li_{aq} = (\delta^7Li_{LiCl} - f_{Li})/(1 - f_{Li}) \quad (\text{Batchsteady} - \text{state}) \tag{10}$$

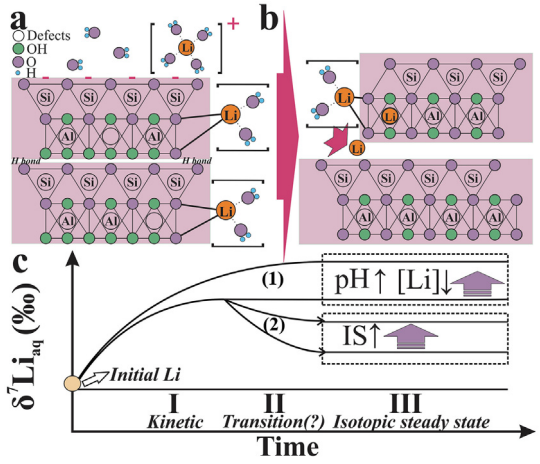

Fig. 4. Conceptual of clay surface Li complexation and isotope fractionation. A schematic illustration of possible processes occurring during Li^+ uptake by kaolinite and subsequent effects on δ^7Li_{aq}. (a) The adsorption of Li^+ onto kaolinite could result in the inner-sphere (chemisorption) and outer-sphere complexations (physisorption). (b) After adsorption, Li may migrate into interlayer spaces and/or occupies structural defects in clay structures. In this case, equilibrium Li isotopic exchange (i.e., the backward reaction) may be inhibited. (c) Conceptual sketch of the sorption of light Li isotopes, resulting in the enrichment of heavy Li isotopes in surrounding solutions. Observed trends imply three successive stages related to solute pH, [Li], and IS. In the plot (c), the path (1) represents the progressive establishment of the stationary isotopic state following a kinetic law. The path (2) reflects successive isotopic behavior, including (I) an initial kinetic fractionation due to preferential diffusion of ^6Li to clay surfaces/interlayers, (II) a gradual transition to isotopic equilibration with surrounding solutions, and (III) a final equilibrium with preferential ^6Li adsorption on clays. In the dashed box, net isotope fractionation between dissolved Li and initial LiCl becomes smaller with reduced Li adsorption, when IS and [Li] are higher, or pH is lower.

$$\delta^7Li_{ad} = \left(\frac{(\delta^7Li_{LiCl} + 1000) \times (1 - (1 - f_{Li}) \times \alpha)}{f_{Li}} - 1000\right);$$

$$\delta^7Li_{aq} = e^{[(\alpha-1)\ln f_{Li} + \ln(\delta^7Li_{LiCl}+1000)]} - 1000 \quad (11)$$

where $\alpha_{ad\text{-}aq}$ is the fractionation factor which defines the magnitude of isotope fractionation of adsorbed Li to dissolved Li, δ^7Li_{LiCl} is the isotope composition of the initial LiCl solution ($5.8 \pm 0.6‰$), and f_{Li} is the proportion of Li lest in solution after releasing from rocks and ($1 - f_{Li}$) denotes the proportion of Li removal by secondary mineral uptake.

The magnitudes of Li isotope fractionation in pH-dependent experiments increase with increasing Li adsorption ratios, and fit the Rayleigh models as opposed to the equilibrium batch models (Fig. 3). Based on the correlation between the fractionation factor α and the adsorption ratio, we estimate the kinetic fractionation factor $\alpha_{ad\text{-}aq}$ to be ~0.992. To exclude potential influence of pH variations in our model fitting, we compared closed-system models using the Li isotopic data from the concentration-control experiments at each pH conditions. At pH = 4.3, Li isotope fractionations fit closed-system batch models, indicating a potential equilibrium isotopic pathway with $\alpha_{ad\text{-}aq} \sim 0.990$. This finding supports our expectation of reversible Li isotopic exchange for outer-sphere complexes under acidic conditions. It is consistent with recent clay synthesis experiments (Hindshaw et al., 2019) showing that Li in outer-sphere complexes is not significantly fractionated relative to the starting solution. Notably, all our Li isotopic data from concentration-controlled experiments under weakly acidic to alkaline conditions confirm closed-system kinetic fractionations when sorption ratios are high (>80%). A recent examination of closed-system basalt sand-natural river interactions of up to 9 months estimated a Rayleigh-type logarithmic relationship between dissolved δ^7Li (i.e., δ^7Li_{aq}) and Li/Na with $\alpha = 0.991$ (Pogge von Strandmann et al., 2019), which supports our findings.

In most cases, Li adsorption onto clays is primarily associated with kinetic isotope fractionations, contrasting the conventional assumption of equilibrium isotope fractionation (Williams and Hervig, 2005; Vigier and Goddéris, 2015) that corresponds to the changes in local atomic environments (Schauble, 2004). In previous studies focusing on clay adsorbed and/or incorporated Li, ^6Li could be preferentially trapped in octahedral sites, following the equilibrium fractionation path, which predicted that ^7Li would be preferentially retained in solutions as tetrahedral aquo-complexes. The proposed equilibrium isotope fractionation mechanism via isomorphic substitutions within octahedral sites of soils depended on both internal (atomic bond strength) and external (e.g., temperature and hydrochemistry) conditions (Vigier et al., 2008; Wimpenny et al., 2015; Hindshaw et al., 2019). For example, the negative correlation between pH and Li isotopic composition in foraminifera has been attributed to changes in Li speciation (Roberts et al., 2018). However, a possible pH control on Li isotope fractionation has not been observed during our clay adsorption experiments nor clay precipitation experiments (Hindshaw et al., 2019), thus solute pH is unlikely to affect Li isotope fractionations. It is noteworthy that the equilibrium fractionation of Li isotopes was verified during clay synthesis based on changes in local Li coordination (Vigier et al., 2008; Hindshaw et al., 2019). The directions and magnitudes of Li isotope fractionations through clay adsorption observed in this study are comparable to those in clay synthetic experiments. Notably, a kinetic Li isotope fractionation was also suggested during stevensite precipitation at high pH (Hindshaw et al., 2019). Therefore, we suggest that both kinetic and equilibrium Li isotope fractionation mechanisms play roles during chemical weathering by Li adsorption onto and Li incorporation into secondary minerals during soil formation.

5.3. Interfacial path for Li isotope fractionation

From this study, there are two types of surface complexation during closed-system Li adsorption onto clays – chemisorption and physisorption, representing the kinetic and equilibrium fractionation processes, respectively (Fig. 4). Hence, clay adsorption occurs predominantly on kaolinite edge surfaces during Rayleigh-type kinetic fractionations ($\alpha \approx 0.992$) and on basal surfaces during equilib-

rium fractionations ($\alpha \approx 0.990$). And the observed $\Delta^7Li_{aq\text{-}ad}$ values probably reflect the net effect of both fractionations. The dominance of the kinetic mechanism at high pH/IS can be attributed to the inner-sphere Li complexation under those conditions. However, a critical question remains: why are covalently adsorbed Li isotopes not rapidly exchanged with the surrounding solution? Rayleigh fractionation implies that adsorbed Li can be rapidly isolated from the solution. Indeed, Li is incorporated into crystallographic defects, and interlayers of gibbsite after adsorption (Wimpenny et al., 2015) and monovalent cations intercalate into kaolinite (Smith et al., 1966). Based on these pieces of evidence, we suggest that adsorbed and kinetically fractionated Li rapidly occupy the structural defects at kaolinite edge surfaces, perhaps even diffusing into the interlayers or deep vacancies after ion dehydration (Fig. 4), where it is then inaccessible to the surrounding aqueous media. Possible Li incorporation may be supported by incomplete desorption after pre-adsorbing on kaolinite (Fig. S5).

Likewise, Hindshaw et al. (2019) proposed that the kinetic-rate processes likely play a role in Li isotope fractionation during phyllosilicate synthesis in high-pH range, similar to Si and Ca isotopes in disequilibrium crystal-growth phenomena (e.g., Nielsen et al., 2012; Geilert et al., 2014). Studies on isotope fractionations within Ca adsorption/desorption processes on soils (Ockert et al., 2013; Brazier et al., 2019) demonstrated that the amplitude of associated isotope fractionation depended on the nature of clay minerals and adsorption site, with both kinetic and equilibrium isotope fractionation being observed. We thus interpret the Li isotopic compositions measured during our experiments to result from three stages of Li adsorption (Fig. 4): (i) two simultaneous kinetic isotope fractionations occur due to the preferential attachment of ^6Li onto kaolinite by inner-sphere and outer-sphere complexation; (ii) chemically adsorbed Li is structurally bound after dehydration, while an equilibrium fractionation continues by physical adsorption of Li from the solute; and (iii) the stationary Li isotopic state is reached and is linked to adsorption ratio. The equilibrium Li isotope fractionation can be reduced by increasing IS, or by decreasing pH or [Li]. Nonetheless, the clay-Li coordination environment cannot be directly detected by common synchrotron-based techniques (e.g., EXAFS) and still remains an open question.

The δ^7Li_{aq} values observed in our experiments were as high as 39.7‰, spanning the wide range of natural observations, and could be quantified using a Rayleigh distillation model with $\alpha_{ad\text{-}aq}$ constant at ~0.992 (Fig. 5a and b). The presence of a similar "distillation" process along the groundwater path has been postulated and simulated by Bohlin and Bickle (2019) for modeling kinetically limited weathering environments. Three distinct mechanisms might explain the observed kinetic Li isotopic behaviors. (I) Hydrated Li ions in the form of $[Li(H_2O)_4]^+$ pass through the clay-fluid boundary layer by diffusion, resulting in significant mass-dependent isotope fractionation due to different diffusion coefficients. (II) The kinetic isotope fractionation of Li predominately depends on surface complexation kinetics in which isotopic exchange is limited by the large activation energy barriers that must be surpassed to break atomic bonds (Schauble, 2004). (III) The kinetic Li isotope fractionation occurs in a reaction-limited regime of surface interaction (DePaolo, 2011). The kinetic fractionation factor α depends on the ratio of net to backward reaction rates. Thus, mechanisms II and III describe a similar mechanism in which the backward reaction becomes negligible compared to the forward reaction once the maximum kinetic isotope fractionation is attained. To distinguish between mechanisms I and III, we compare our data to a molecular dynamic simulation using theoretical diffusion (Bourg et al., 2010) and ion desolvation (Hofmann et al., 2012) parameters for Li isotopes (Fig. 5c). Our data agree with the theoretical ion desolvation model with α of 0.9925 ± 0.0014, corresponding to a quantum–mechanical mechanism of complexation and subsequent incorporation (Hofmann et al., 2012). The result of desorption experiments implies that Li clay adsorption is not fully reversible (Fig. S5). We infer that a loose water solvation shell surrounds hydrated Li; rate-limited dehydration thus causes kinetic effects during interfacial interactions.

5.4. Implications

A critical finding of this study is that the equilibrium fractionation of Li isotopes occurs through outer-sphere complexation, predominately under low pH/IS conditions. Because physically fixed outer-sphere Li should maintain four-fold coordination (similar to the four-fold coordinated hydrated Li-ions), Li isotopes are unlikely to be fractionated during outer-sphere complexation. Nevertheless, observable metal stable isotope fractionations have been reported for outer-sphere complexes. For example, Brazier et al. (2019) highlighted the importance of interlayer charges in determining the magnitude of weakly-bonded Ca (outer-sphere) isotope fractionations (Brazier et al., 2019). Hence, we postulate that electrostatic interaction affects the solvation number, though this requires further laboratory and theoretical examination. Increasingly significant kinetic control on isotopic fraction with increasing inner-sphere Li complexation (i.e., at higher pH) may be important in natural systems (e.g., rivers and oceans) under neutral to alkaline conditions. As clay sorption usually occurs prior to lattice incorporation (Pogge von Strandmannet al., 2017b), kinetic Li isotopic fractions may be preserved during soil formation. Furthermore, our interpretations are consistent with global riverine observations (Fig. 5d). The good agreement between observed and experimental δ^7Li values suggests that kinetically driven adsorption and incorporation may be a primary mechanism driving natural isotope fractionations.

The consistency between our results and natural observations demonstrates the critical role of kinetic controls on Li isotope fractionations during chemical weathering, although it invokes another question: can river systems be treated as closed systems? At first glance, riverine systems are open systems because they receive influxes from bedrock weathering and erosion, deposit sediments during transport, and, subsequently, provide outfluxes to reservoirs as oceans. However, it takes time to follow the entire source-to-sink pathway, from bedrock via weathering pro-

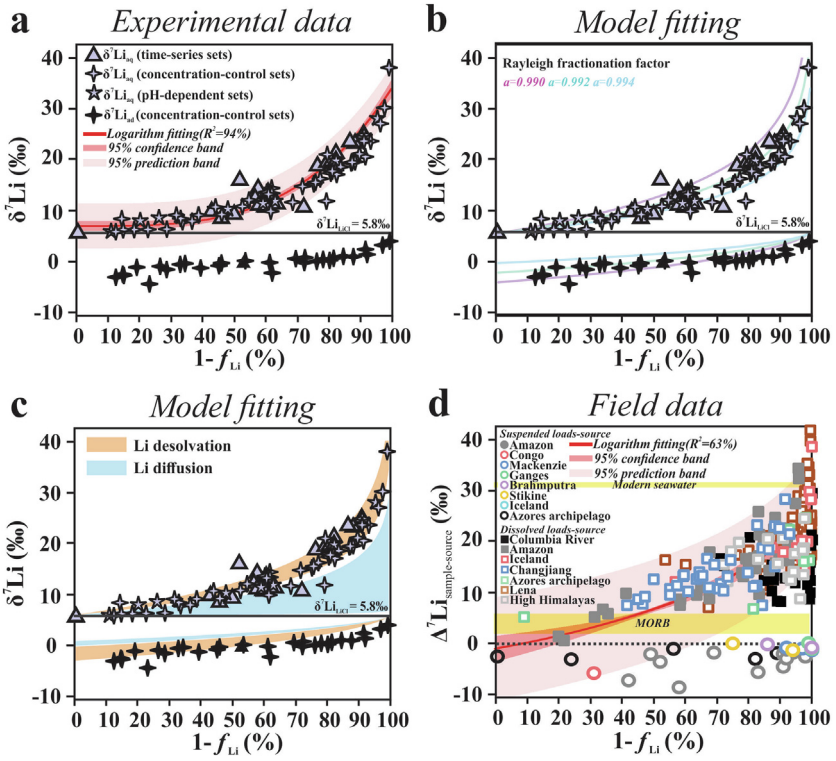

Fig. 5. Experiment and field Li isotope data compilation and integrated modeling results. (a) Exponential fitting and (b) Rayleigh distillation model based on linear fitting to our data using fractionation factor $\alpha_{ad\text{-}aq}$ from 0.990 to 0.994. A closed-system Rayleigh distillation model produces the best fit with the $\alpha_{ad\text{-}aq} \approx 0.992$, and agree with the range of δ^7Li values observed in continental to marine environments (data refer to Tomascak et al., 2016 and references therein). The initial Li isotopic compositions of the LiCl and pristine kaolinite are 5.8‰ and 0.2‰, respectively. (c) Molecular dynamic simulations of Li isotope fractionation via Li desolvation in aqueous systems (fractionation factor $\alpha = 0.9925 \pm 0.0014$; Hofmann et al., 2012) and Li diffusion in liquid water (diffusivity empirical constant, $\beta = 0.0171 \pm 0.0159$, Bourg et al., 2010). (d) Rayleigh distillation modeling of data from a literature compilation of river suspended and dissolved loads (data summarized in Tables S4-S5) of global riverine systems. MORB: the mid-ocean-ridge basalts. Long-term analytical uncertainty on δ^7Li (2SD = 0.6‰) is smaller than the symbol size. f_{Li} represents the fraction of Li remaining in the liquid after lithology correction, normalized to the Li composition of source rock. If $(1\text{-}f_{Li}) = 1$, chemical weathering is congruent. The percentage of Li adsorption from solution $(1\text{-}f_{Li})$ is calculated using $(Li/Na)_{source}/(Li/Na)_{dissolved}$ and $(Li/Al)_{suspended}/(Li/Al)_{source}$, corresponding to Li re-incorporated into soils after initial release from silicate rocks by weathering. Plotted field data refer to the data of Amazon rivers (Dellinger et al., 2015, 2017), Congo rivers (Dellinger et al., 2017), Mackenzie rivers (Millot et al., 2010), Ganges rivers (Pogge von Strandmannet al., 2017b), Brahmputra rivers (Dellinger et al., 2014), Stikine rivers (Dellinger et al., 2017), Iceland rivers (Vigier et al., 2009; Pogge von Strandmann et al., 2016), Azores archipelago (Pogge von Strandmann et al., 2010), Changjiang rivers (Gou et al., 2019; Ma et al., 2020), Columbia rivers (Liu et al., 2015), Lena rivers (Murphy et al., 2019) and high Himalaya rivers (Kısakűrek et al., 2005). Analytical uncertainties of Li isotope analysis in mentioned publications are within the symbol size in the Y-axis.

files, to groundwaters and rivers (with potential floodplain storage), and to the marine realm. The dissolved and suspended loads travel together within rivers, especially in transport-limited weathering regions (e.g., floodplains) characterized by long water residence times (days to weeks, or longer) and low sedimentation rates. For example, the alluvial plains and vast riparian zones of rivers that carry even a low amount of suspended clays can certainly be considered as closed systems. In such cases, it is appropriate to treat the dissolved and suspended loads as being in a semi-closed system. Assuming that kinetic Li isotope fractionations are ubiquitous on Earth's surfaces, rivers potentially exert a more prominent impact on oceanic isotope mass balance compared with early expectations. It is consistent with the interpretation that enhanced weathering during the Cenozoic promoted heavy δ^7Li inputs into the oceans, contributing to a ~9‰ increase of oceanic δ^7Li (Misra and Froelich, 2012; Wanner et al., 2014). Our findings demonstrate kinetically controlled Li isotope fractionation during uptake by kaolinite, refining Li isotopic systematic as tracers of weathering and climate. This work also establishes δ^7Li as a sensitive index for clay formation during chemical weathering and also demonstrates that natural observations on Li isotope records cannot be simply treated as representing constant isotope fractionation level (e.g., Bouchez et al., 2013; Bohlin and Bickle, 2019). Previous quantitative interpretations of natural Li isotopic records thus may require refinements to account for low-temperature kinetic Li isotope fractionations during chemical weathering.

6. CONCLUSIONS

We performed systematic laboratory batch experiments to explore the mechanism and quantify the magnitude of Li isotope fractionation during the adsorption of kaolinite - a common weathering product. According to our systematic experiments, including time series-, pH- and concentration-control sets, the liquid-solid isotopic variations range from ~0‰ to 36‰, with 10–99% starting solute Li being adsorbed. Li was removed by inner-sphere/outer-sphere surface complexation, likely followed by lattice occupation. We demonstrated that Li isotope fractionation during kaolinite uptake could be best described using a closed-system Rayleigh distillation model ($\alpha \sim 0.992$). These results are also consistent with the theoretical calculation of Li^+ desolvation ($\alpha \sim 0.9925$), and field observation of worldwide rivers. We conclude that the same kinetic isotope fractionation mechanism may be responsible for the wide ranges of Li isotopic signatures on Earth's surfaces. The importance of this finding includes that soil formation associated with kinetic controls may be the main driver for pronounced Li isotope fractionation, particularly in transport-limited weathering regions and, by extension, the continental-marine Li isotopic fluctuations during weathering over geological timescales.

Declaration of Competing Interest

The authors declare that they have no known competing financial interests or personal relationships that could have appeared to influence the work reported in this paper.

ACKNOWLEDGMENTS

We thank Laura Wasylenki and Julie Barzyk for helpful discussions and improving the manuscript. We thank Linda Godfrey for her assistance with MC-ICP-MS analyses. We are especially grateful to Dr. P. B. Tomascak, the two anonymous reviewers and the editor Dr. O.S. Pokrovsky for suggesting significant improvements to this manuscript.

FUNDING

X.-M.L. acknowledges funding support from an NSF Career Award (EAR-1848153) and US Army Research Office grant W911NF-17-2-0028.

AUTHOR CONTRIBUTIONS

X.-M.L. designed the project. W.S.L. performed experiments, statistical analyses, and model development. Both authors contributed to the interpretation of the results and writing of the manuscript.

DATA AND MATERIALS AVAILABILITY

All data needed to evaluate the conclusions in the paper are present in the text and the Supplementary Materials. Additional data related to this paper could be requested from the authors.

APPENDIX A. SUPPLEMENTARY DATA

Supplementary data to this article can be found online at https://doi.org/10.1016/j.gca.2020.06.025.

REFERENCES

Bagard M. L., West A. J., Newman K. and Basu A. R. (2015) Lithium isotope fractionation in the Ganges-Brahmaputra floodplain and implications for groundwater impact on seawater isotopic composition. *Earth Planet. Sci. Lett.* **432**, 404–414.

Bencala K. E., McKnight D. M. and Zellweger G. W. (1990) Characterization of transport in an acidic and metal-rich mountain stream based on a lithium tracer injection and simulations of transient storage. *Water Resour. Res.* **26**, 989–1000.

Bogatko S., Claeys P., De Proft F. and Geerlings P. (2013) Li^+ speciation and the use of 7Li/6Li isotope ratios for ancient climate monitoring. *Chem. Geol.* **357**, 1–7.

Bohlin M. S. and Bickle M. J. (2019) The reactive transport of Li as a monitor of weathering processes in kinetically limited weathering regimes. *Earth Planet. Sci. Lett.* **511**, 233–243.

Bouchez J., Von Blanckenburg F. and Schuessler J. A. (2013) Modeling novel stable isotope ratios in the weathering zone. *Am. J. Sci.* **313**, 267–308.

Bourg I. C., Richter F. M., Christensen J. N. and Sposito G. (2010) Isotopic mass dependence of metal cation diffusion coefficients in liquid water. *Geochim. Cosmochim. Acta* **74**, 2249–2256.

Brazier J. M., Schmitt A. D., Gangloff S., Pelt E., Chabaux F. and Tertre E. (2019) Calcium isotopic fractionation during adsorption onto and desorption from soil phyllosilicates (kaolinite, montmorillonite and muscovite). *Geochim. Cosmochim. Acta* **250**, 324–347.

Bryan A. L., Dong S., Wilkes E. B. and Wasylenki L. E. (2015) Zinc isotope fractionation during adsorption onto Mn oxyhydroxide at low and high ionic strength. *Geochim. Cosmochim. Acta* **157**, 182–197.

Dellinger M., Bouchez J., Gaillardet J., Faure L. and Moureau J. (2017) Tracing weathering regimes using the lithium isotope composition of detrital sediments. *Geology* **45**, 411–414.

Dellinger M., Gaillardet J., Bouchez J., Calmels D., Galy V., Hilton R. G., Louvat P. and France-Lanord C. (2014) Lithium isotopes in large rivers reveal the cannibalistic nature of modern continental weathering and erosion. *Earth Planet. Sci. Lett.* **401**, 359–372.

Dellinger M., Gaillardet J., Bouchez J., Calmels D., Louvat P., Dosseto A., Gorge C., Alanoca L. and Maurice L. (2015) Riverine Li isotope fractionation in the Amazon River basin controlled by the weathering regimes. *Geochim. Cosmochim. Acta* **164**, 71–93.

DePaolo D. J. (2011) Surface kinetic model for isotopic and trace element fractionation during precipitation of calcite from aqueous solutions. *Geochim. Cosmochim. Acta* **75**, 1039–1056.

Dosseto A., Vigier N., Joannes-Boyau R., Moffat I., Singh T. and Srivastava P. (2015) Rapid response of silicate weathering rates to climate change in the Himalaya. *Geochemical Perspect. Lett.* **1**, 10–19.

Freundlich H. (1928) *Colloid and Capillary Chemistry*. E.P. Dutton and Co, New York.

Geilert S., Vroon P. Z., Roerdink D. L., Van Cappellen P. and van Bergen M. J. (2014) Silicon isotope fractionation during abiotic silica precipitation at low temperatures: Inferences from flow-through experiments. *Geochim. Cosmochim. Acta* **142**, 95–114.

Gou L. F., Jin Z., Pogge von Strandmann P. A. E., Li G., Qu Y. X., Xiao J., Deng L. and Galy A. (2019) Li isotopes in the middle Yellow River: Seasonal variability, sources and fractionation. *Geochim. Cosmochim. Acta* **248**, 88–108.

Guinoiseau D., Gélabert A., Moureau J., Louvat P. and Benedetti M. F. (2016) Zn Isotope fractionation during sorption onto kaolinite. *Environ. Sci. Technol.* **50**, 1844–1852.

Hathorne E. C. and James R. H. (2006) Temporal record of lithium in seawater: A tracer for silicate weathering? *Earth Planet Sci. Lett.* **246**, 393–406.

Heidmann I., Christl I. and Kretzschmar R. (2005) Sorption of Cu and Pb to kaolinite-fulvic acid colloids: Assessment of sorbent interactions. *Geochim. Cosmochim. Acta* **69**, 1675–1686.

Heimsath A. M., DiBiase R. A. and Whipple K. X. (2012) Soil production limits and the transition to bedrock-dominated landscapes. *Nat. Geosci.* **5**, 210–214.

Hindshaw R. S., Tosca R., Goût T. L., Farnan I., Tosca N. J. and Tipper E. T. (2019) Experimental constraints on Li isotope fractionation during clay formation. *Geochim. Cosmochim. Acta* **250**, 219–237.

Ho Y. S. and McKay G. (1999) Pseudo-second order model for sorption processes. *Process Biochem.* **34**, 451–465.

Hofmann A. E., Bourg I. C. and DePaolo D. J. (2012) Ion desolvation as a mechanism for kinetic isotope fractionation in aqueous systems. *Proc. Natl. Acad. Sci. U. S. A.* **109**, 18689–18694.

Huh Y., Chan L. H. and Edmond J. M. (2001) Lithium isotopes as a probe of weathering processes: Orinoco River. *Earth Planet. Sci. Lett.* **194**, 189–199.

Huh Y., Chan L. H., Zhang L. and Edmond J. M. (1998) Lithium and its isotopes in major world rivers: implications for weathering and the oceanic budget. *Geochim. Cosmochim. Acta* **62**, 2039–2051.

John C. M., Mutti M. and Adatte T. (2003) Mixed carbonate-siliciclastic record on the North African margin (Malta) - Coupling of weathering processes and mid Miocene climate. *Bull. Geol. Soc. Am.* **115**, 217–229.

Kısakűrek B., Widdowson M. and James R. H. (2004) Behaviour of Li isotopes during continental weathering: The Bidar laterite profile, India. *Chem. Geol.* **212**, 27–44.

Kump L. R., Brantley S. L. and Arthur M. A. (2000) Chemical Weathering, Atmospheric CO_2, and Climate. *Annu. Rev. Earth Planet. Sci.* **28**, 611–667.

Lagergren S. K. (1898) About the theory of so-called adsorption of soluble substances. *Sven. Vetenskapsakad. Handingarl* **24**, 1–39.

Langmuir I. (1918) The adsorption of gases on plane surfaces of glass, mica and platinum. *J. Am. Chem. Soc.* **40**, 1361–1403.

Lechler M., Pogge von Strandmann P. A. E., Jenkyns H. C., Prosser G. and Parente M. (2015) Lithium-isotope evidence for enhanced silicate weathering during OAE 1a (Early Aptian Selli event). *Earth Planet. Sci. Lett.* **432**, 210–222.

Lee S., Anderson P. R., Bunker G. B. and Karanfil C. (2004) EXAFS study of Zn sorption mechanisms on montmorillonite. *Environ. Sci. Technol.* **38**, 5426–5432.

Li G. and West A. J. (2014) Evolution of Cenozoic seawater lithium isotopes: Coupling of global denudation regime and shifting seawater sinks. *Earth Planet. Sci. Lett.* **401**, 284–293.

Li W., Liu X. M. and Godfrey L. V. (2019) Optimisation of Lithium Chromatography for Isotopic Analysis in Geological Reference Materials by MC-ICP-MS. *Geostand. Geoanalytical Res.* **43**, 261–276.

Lin J., Liu Y., Hu Z., Yang L., Chen K., Chen H., Zong K. and Gao S. (2016) Accurate determination of lithium isotope ratios by MC-ICP-MS without strict matrix-matching by using a novel washing method. *J. Anal. At. Spectrom.* **31**, 390–397.

Liu X. M. and Li W. (2019) Optimization of lithium isotope analysis in geological materials by quadrupole ICP-MS. *J. Anal. At. Spectrom.* **34**, 1708–1717.

Liu X. M., Wanner C., Rudnick R. L. and McDonough W. F. (2015) Processes controlling δ^7Li in rivers illuminated by study of streams and groundwaters draining basalts. *Earth Planet. Sci. Lett.* **409**, 212–224.

Low M. J. D. (1960) Kinetics of chemisorption of gases on solids. *Chem. Rev.* **60**, 267–312.

Ma T., Weynell M., Li S. L., Liu Y., Chetelat B., Zhong J., Xu S. and Liu C. Q. (2020) Lithium isotope compositions of the Yangtze River headwaters: Weathering in high-relief catchments. *Geochim. Cosmochim. Acta* **280**, 46–65.

Millot, R., Girard, J.P., 2007. Lithium isotope fractionation during adsorption onto mineral surfaces. In: Clays Nat. Eng. Barriers Radioact. Waste Confin. 3rd Int. Meet., 307–308. Available at: http://www.andra.fr/lille2007/abstract_lille2007/donnees/pdf/307_308_P_GM_6.pdf.

Millot R., Vigier N. and Gaillardet J. (2010) Behaviour of lithium and its isotopes during weathering in the Mackenzie Basin, Canada. *Geochim. Cosmochim. Acta* **74**, 3897–3912.

Misra S. and Froelich P. N. (2012) Lithium isotope history of cenozoic seawater: Changes in silicate weathering and reverse weathering. *Science (80-.)* **335**, 818–823.

Murphy M. J., Porcelli D., Pogge von Strandmann P. A. E., Hirst C. A., Kutscher L., Katchinoff J. A., Mörth C. M., Maximov T. and Andersson P. S. (2019) Tracing silicate weathering processes in the permafrost-dominated Lena River watershed using lithium isotopes. *Geochim. Cosmochim. Acta* **245**, 154–171.

Nielsen L. C., DePaolo D. J. and De Yoreo J. J. (2012) Self-consistent ion-by-ion growth model for kinetic isotopic fractionation during calcite precipitation. *Geochim. Cosmochim. Acta* **86**, 166–181.

Ockert C., Gussone N., Kaufhold S. and Teichert B. M. A. (2013) Isotope fractionation during Ca exchange on clay minerals in a marine environment. *Geochim. Cosmochim. Acta* **112**, 374–388.

Peacock C. L. and Sherman D. M. (2004) Copper(II) sorption onto goethite, hematite and lepidocrocite: A surface complexation model based on ab initio molecular geometries and EXAFS spectroscopy. *Geochim. Cosmochim. Acta* **68**, 2623–2637.

Penniston-Dorland S., Liu X. M. and Rudnick R. L. (2017) Lithium isotope geochemistry. *Non-Traditional Stable Isotopes Walter de Gruyter GmbH.*, 165–218.

Pistiner J. S. and Henderson G. M. (2003) Lithium-isotope fractionation during continental weathering processes. *Earth Planet. Sci. Lett.* **214**, 327–339.

Pogge von Strandmann P. A. E., Burton K. W., James R. H., van Calsteren P. and Gislason S. R. (2010) Assessing the role of climate on uranium and lithium isotope behaviour in rivers draining a basaltic terrain. *Chem. Geol.* **270**, 227–239.

Pogge von Strandmann P. A. E., Fraser W. T., Hammond S. J., Tarbuck G., Wood I. G., Oelkers E. H. and Murphy M. J. (2019) Experimental determination of Li isotope behaviour during basalt weathering. *Chem. Geol.* **517**, 34–43.

Pogge von Strandmann P. A. E., Frings P. J. and Murphy M. J. (2017) Lithium isotope behaviour during weathering in the Ganges Alluvial Plain. *Geochim. Cosmochim. Acta* **198**, 17–31.

Pogge von Strandmann P. A. E., Desrochers A., Murphy M. J., Finlay A. J., Selby D. and Lenton T. M. (2017) Global climate stabilisation by chemical weathering during the Hirnantian glaciation. *Geochemical Perspect. Lett.* **3**, 230–237.

Pogge von Strandmann P. A. E. and Henderson G. M. (2015) The Li isotope response to mountain uplift. *Geology* **43**, 67–70.

Pogge von Strandmann P. A., Burton K. W., Opfergelt S., Eiríksdóttir E. S., Murphy M. J., Einarsson A. and Gislason S. R. (2016) The effect of hydrothermal spring weathering processes and primary productivity on lithium isotopes: Lake Myvatn, Iceland. *Chem. Geol.* **445**, 4–13.

Pogge von Strandmann P. A. E., James R. H., van Calsteren P., Gíslason S. R. and Burton K. W. (2008) Lithium, magnesium and uranium isotope behaviour in the estuarine environment of basaltic islands. *Earth Planet. Sci. Lett.* **274**, 462–471.

Pogge Von Strandmann P. A. E., Jenkyns H. C. and Woodfine R. G. (2013) Lithium isotope evidence for enhanced weathering during Oceanic Anoxic Event 2. *Nat. Geosci.* **6**, 668–672.

Roberts J., Kaczmarek K., Langer G., Skinner L. C., Bijma J., Bradbury H., Turchyn A. V., Lamy F. and Misra S. (2018) Lithium isotopic composition of benthic foraminifera: A new proxy for paleo-pH reconstruction. *Geochim. Cosmochim. Acta* **236**, 336–350.

Rudolph W., Brooker M. H. and Pye C. C. (1995) Hydration of lithium ion in aqueous solution. *J. Phys. Chem.* **99**, 3793–3797.

Schauble E. A. (2004) Applying stable isotope fractionation theory to new systems. *Rev. Mineral. Geochemistry* **55**, 65–111.

Smith D. L., Milford M. H. and Zuckerman J. J. (1966) Mechanism for intercalation of kaolinite by alkali acetates. *Science* **153**, 741–743.

Srihari V. and Das A. (2008) The kinetic and thermodynamic studies of phenol-sorption onto three agro-based carbons. *Desalination* **225**, 220–234.

Strawn D. G. and Sparks D. L. (1999) The use of XAFS to distinguish between inner- and outer-sphere lead adsorption complexes on montmorillonite. *J. Colloid Interface Sci.* **216**, 257–269.

Tabor N. J., Montanez I. P. and Southard R. J. (2002) Paleoenvironmental reconstruction from chemical and isotopic compositions of Permo-Pennsylvanian pedogenic minerals. *Geochim. Cosmochim. Acta* **66**, 3093–3107.

Tomascak, P.B., Magna, T., Dohmen, R., 2016. Advances in Lithium Isotope Geochemistry., Available at: http://link.springer.com/10.1007/978-3-319-01430-2.

Tomascak P. B., Tera F., Helz R. T. and Walker R. J. (1999) The absence of lithium isotope fractionation during basalt differentiation: New measurements by multicollector sector ICP-MS. *Geochim. Cosmochim. Acta* **63**, 907–910.

Tombácz E. and Szekeres M. (2006) Surface charge heterogeneity of kaolinite in aqueous suspension in comparison with montmorillonite. *Appl. Clay Sci.* **34**, 105–124.

Vasconcelos I. F., Haack E. A., Maurice P. A. and Bunker B. A. (2008) EXAFS analysis of cadmium(II) adsorption to kaolinite. *Chem. Geol.* **249**, 237–249.

Vigier N., Decarreau A., Millot R., Carignan J., Petit S. and France-Lanord C. (2008) Quantifying Li isotope fractionation during smectite formation and implications for the Li cycle. *Geochim. Cosmochim. Acta* **72**, 780–792.

Vigier N., Gislason S. R., Burton K. W., Millot R. and Mokadem F. (2009) The relationship between riverine lithium isotope composition and silicate weathering rates in Iceland. *Earth Planet. Sci. Lett.* **287**, 434–441.

Vigier N. and Goddéris Y. (2015) A new approach for modeling Cenozoic oceanic lithium isotope paleo-variations: The key role of climate. *Clim. Past* **11**, 635–645.

Wang Q. L., Chetelat B., Zhao Z. Q., Ding H., Li S. L., Wang B. L., Li J. and Liu X. L. (2015) Behavior of lithium isotopes in the Changjiang River system: Sources effects and response to weathering and erosion. *Geochim. Cosmochim. Acta* **151**, 117–132.

Wanner C., Sonnenthal E. L. and Liu X. M. (2014) Seawater δ7Li: A direct proxy for global CO2 consumption by continental silicate weathering? *Chem. Geol.* **381**, 154–167.

Weynell M., Wiechert U. and Schuessler J. A. (2017) Lithium isotopes and implications on chemical weathering in the catchment of Lake Donggi Cona, northeastern Tibetan Plateau. *Geochim. Cosmochim. Acta* **213**, 155–177.

Wilke R. J. and Dayal R. (1982) The behavior of iron, manganese and silicon in the Peconic River estuary, New York. *Estuar. Coast. Shelf Sci.* **15**, 577–586.

Willenbring J. K. and Von Blanckenburg F. (2010) Long-term stability of global erosion rates and weathering during late-Cenozoic cooling. *Nature* **465**, 211–214.

Williams L. B. and Hervig R. L. (2005) Lithium and boron isotopes in illite-smectite: The importance of crystal size. *Geochim. Cosmochim. Acta* **69**, 5705–5716.

Wimpenny J., Colla C. A., Yu P., Yin Q. Z., Rustad J. R. and Casey W. H. (2015) Lithium isotope fractionation during uptake by gibbsite. *Geochim. Cosmochim. Acta* **168**, 133–150.

Yamaji K., Makita Y., Watanabe H., Sonoda A., Kanoh H., Hirotsu T. and Ooi K. (2001) Theoretical estimation of lithium isotopic reduced partition function ratio for lithium ions in aqueous solution. *J. Phys. Chem. A* **105**, 602–613.

Associate editor: Oleg Pokrovsky